Journal of Power Sources 337 (2017) 180–188

Contents lists available at ScienceDirect

Journal of Power Sources

journal homepage: www.elsevier.com/locate/jpowsour

Free-standing electrodes composed of carbon-coated $Li_4Ti_5O_{12}$ nanosheets and reduced graphene oxide for advanced sodium ion batteries

Guobao Xu [a], Ye Tian [a], Xiaolin Wei [a], Liwen Yang [a, b, *], Paul K. Chu [b, **]

[a] Hunan Key Laboratory of Micro-Nano Energy Materials and Devices, School of Physics and Optoelectronics, Xiangtan University, Hunan 411105, China
[b] Department of Physics and Materials Science, City University of Hong Kong, Tat Chee Avenue, Kowloon, Hong Kong, China

HIGHLIGHTS

- A general and scalable approach for free-standing and flexible electrodes is demonstrated.
- Free-standing electrodes composed of carbon-coated LTO nanosheets and RGO are fabricated.
- The free-standing LTO-C/RGO anode demonstrates superior Na storage performance.

ARTICLE INFO

Article history:
Received 1 September 2016
Received in revised form
23 October 2016
Accepted 25 October 2016
Available online 3 November 2016

Keywords:
Sodium ion battery
Free-standing
$Li_4Ti_5O_{12}$
Graphene
Nanosheets

ABSTRACT

A free-standing electrode composed of carbon-coated $Li_4Ti_5O_{12}$ nanosheets and reduced graphene oxide (designated as LTO-C/RGO) is fabricated for Na storage by modified vacuum filtration and subsequent annealing. In this process, graphene oxide with negative charges and LTO-C nanosheets with abundant charged ions are self-assembled into the nanocomposite based on the screening effect of electrostatic repulsion. The unique structure of the confined LTO-C nanosheets in a highly conductive interconnected RGO network not only promotes the reaction kinetics and structural stability of the electrodes during Na^+ insertion/extraction, but also provides plenty of interfacial sites for Na^+ adsorption giving rise to additional interfacial Na storage. The free-standing LTO-C/RGO anode for sodium ion battery exhibits a high capacity of 166 $mAhg^{-1}$ at 1 C, good rate capability of 98.7 $mAhg^{-1}$ at 5 C, and superior cyclic performance of 114 $mAhg^{-1}$ at 2 C after 600 cycles. The materials boasting superior Na storage have large potential in high-performance sodium ion batteries in portable, flexible and wearable electronics.

1. Introduction

With the rise of portable, flexible and wearable electronics, it is urgent to develop high-performance flexible energy storage devices such as batteries and supercapacitors [1,2]. Room-temperature sodium ion batteries (SIBs) have attracted increasing attention because of their similar electrochemical properties with lithium-ion batteries (LIBs) in addition to low cost and environmental friendliness [3,4]. The characteristics of batteries such as flexibility, specific capacity, and rate capability are mainly determined by electrode materials [5]. Therefore it is of importance to search for suitable electrode materials with appropriate flexibility for SIBs.

Spinel $Li_4Ti_5O_{12}$ (LTO) has been investigated as a promising electrode material in LIBs on account of its high charging/discharging voltage plateau of 1.55 V vs. Li/Li^+ as well as zero-strain feature towards lithium insertion/extraction and environmental benignity [6,7]. Recently, a theoretical capacity of 175 $mAhg^{-1}$ has been reported [8–10] and the relatively large storage voltage of 0.91 V versus Na makes it safer than hard carbon as an anode material in high-performance SIBs. Nevertheless, its practical application of SIBs has been hampered because of the unsatisfactory rate capability due to poor electrical conductivity (10^{-13} S cm^{-1}) and slow Na^+ diffusion coefficient of LTO (10^{-16} cm^2s^{-1}) [11]. Strategies to improve electrochemical performance

* Corresponding author. Hunan Key Laboratory of Micro-Nano Energy Materials and Devices, School of Physics and Optoelectronics, Xiangtan University, Hunan 411105, China.
** Corresponding author.
E-mail addresses: ylwxtu@xtu.edu.cn (L. Yang), paul.chu@cityu.edu.hk (P.K. Chu).

http://dx.doi.org/10.1016/j.jpowsour.2016.10.088
0378-7753/

have mainly focused on fabricating composites composed of nano/microstructured LTO and highly conductive carbonaceous materials such as carbon nanotubes and graphene, because the former shortens the electron and Na ion transport lengths [12–14] and the latter enables more effective electron transport [15–20]. For example, Kim et al. developed an ionic-exchange route to synthesize carbon-coated LTO nanowires [15] and Chen et al. prepared composite aerogel of porous LTO nanofibers confined in a highly conductive interconnected graphene framework [20]. As expected, these LTO/carbon nanocomposites deliver improved performance in SIBs. However, most of them adopt the traditional electrode configuration consisting of an electrically insulating polymer binder, conductive additive, and active materials on the metallic current collector foil produced by a standard but tedious slurry-coating process. The conductive additives and insulating binders not only increase the total cost and weight of the SIBs, but also adversely affect the electrode performance including energy and power densities [21,22]. Consequently, it is desirable to construct free-standing and flexible LTO/carbon nanocomposites to spur the application of LTO-based materials to high-performance SIBs.

LTO nanosheets possess large discharge capacity and improved rate capability due to larger exposed specific surface area resulting in more active reactions and shorter path lengths thereby enabling highly efficient electron/ion transport [14,23–26]. Furthermore, surface modification by ultrathin carbon encapsulation around the LTO nanostructures is an effective method to improve the rate capability and cycling performance of LTO electrodes due to enhanced charge transfer/collection kinetics and interfacial stability between the solid electrode and electrolyte [17,27,28]. The unique two-dimensional (2D) structure and physical properties of graphene and its derivatives make them the most suitable building blocks to anchor electroactive materials to prepare free-standing and binder-free flexible electrodes [25,29]. Despite recent investigations on LTO nanosheets, carbon-coated LTO, and LTO/graphene composites, there have been few studies on the fabrication and Na storage performance of free-standing and flexible electrodes consisting of carbon-coated LTO nanosheets and graphene-based scaffolds. In this work, a unique free-standing electrode composed of highly-crystalline carbon-coated LTO nanosheets and reduced graphene oxide (designated as LTO-C/RGO) is designed and fabricated for high-performance SIBs. During the fabrication, graphene oxide (GO) nanosheets with negative charges and LTO-C nanosheets in a solution with high ionic strength prepared with 1 M NH_4HCO_3 are self-assembled into the nanocomposite by utilizing electrostatic repulsion. Subsequent vacuum filtration forms the freestanding flexible nanocomposite film and further annealing reduces the GO and strengthens the internal structure forming robust and flexible LTO-C/RGO electrode. The developed free-standing electrodes for SIBs have desirable electrochemical performance such as a high reversible capacity of 166 $mAhg^{-1}$ at 1 C, good rate capability of 98.7 $mAhg^{-1}$ at 5 C, and superior cyclic performance of 114 $mAhg^{-1}$ at 2 C after 600 cycles.

2. Experimental details

2.1. Synthesis of LTO nanosheets

The LTO nanosheets were prepared by a modified hydrothermal method and annealing [28]. In the typical synthesis, 1.7 ml (5 mM) of tetrabutyl titanate, 0.189 g of $LiOH \cdot H_2O$, and an appropriate amount of $GdCl_3.6H_2O$ were mixed in 20 ml of ethanol at room temperature. The solution was mixed under magnetic stirring for 24 h and 25 ml of deionized water were added. After stirring for 0.5 h, the solution was transferred to a 50 ml Teflon-lined stainless autoclave and inserted into an oven. The hydrothermal reaction proceeded at 180 °C for 36 h to obtain the $Li_{1.81}H_{0.19}Ti_2O_5 \bullet xH_2O$ (designated as H-LTO) precursor. The white H-LTO precursor on the bottom of the reactor was collected, washed with ethanol 3 times, and dried at 80 °C for 6 h. Finally, the white H-LTO precursor was heated to 700 °C for 6 h in a horizontal tube furnace in air to obtain the LTO nanosheets.

2.2. Synthesis of carbon-coated LTO nanosheets

The LTO-C nanosheets were prepared by controlling the amount of carbon precursor (D(t)-glucose monohydrate) as described in Section 2.1. The H-LTO precursor was first prepared and then 200 mg of the H-LTO precursor were dispersed in 10 ml of ethanol under magnetic stirring to form Solution A. D(t)-glucose monohydrate with an amount corresponding to nominal 5 wt% of the H-LTO precursor was dissolved in 5 ml of ethanol to produce Solution B. Solution B was added dropwise to Solution A under stirring, followed by slow evaporation into a slurry at 80 °C. The slurry was heated under Ar/H_2 (5%) atmosphere to 700 °C for 6 h to produce the carbon-coated LTO (designated as LTO-C) nanosheets.

2.3. Fabrication of free-standing LTO-C/RGO film

The LTO-C nanosheets were dispersed in a 100 ml solution containing 1 M NH_4HCO_3 to form Solution A, and graphene oxide synthesized by oxidizing graphite by the modified Hummers method were dispersed in 100 ml of deonized water to produce Solution B. Solution A was added dropwise to Solution B under magnetic stirring. The black fluffy composite sank to the bottom in 10 min without stirring. The black composite was collected by vacuum filtration with a microporous membrane with a pore size of 0.45 μm. After drying at 60 °C for 6 h, the materials were peeled off from the microporous membrane and annealed under Ar/H_2 (5%) at 700 °C for 2 h to produce the free-standing LTO-C/RGO film. The thickness of the free-standing LTO-C/RGO film was controlled by adjusting the content of vacuum-filtered fluffy composite.

2.4. Materials characterization

The crystal structure of the samples was determined by X-ray diffraction (XRD) using a Cu K_α radiation (λ = 0.154 nm). The morphology and microstructure of the samples were characterized using scanning electron microscopy (SEM) and transmission electron microscopy (TEM, JEOL 2100) equipped with selected-area electron diffraction (SAED) and energy dispersive X-ray spectrometry (EDS, Oxford). X-ray photoelectron spectroscopy (XPS) was performed using an Al K_α source (Kratos Analytical Ltd., UK) and the C 1s binding energy of 284.8 eV was used in the calibration. Fourier-transform infrared (FTIR) spectroscopy was conducted on a FTS-3000 Fourier transform infrared spectrophotometer. The Raman scattering spectra were recorded on a Renishaw inVia system at a laser wavelength λ of 532 nm. The thermogravimetric analysis (TGA) was carried out using a TGA 2050 thermogravimetric analyzer to determine the amounts of LTO in the flexible samples.

2.5. Electrochemical characterization

The electrochemical tests were conducted on the two-electrode CR2032 type coin cells. The free-standing and flexible films were directly used as the working electrodes. The coin cells were assembled in an argon-filled glove box with a metallic sodium foil as the counter electrode and glass fiber (Whatman GF/D) as the separator in the sodium cells. The electrolyte was 1 M $NaClO_4$ in a 1:1 (volume) mixture of ethylene carbonate/propylene carbonate. The discharging/charging experiments were performed at various

current densities over a voltage range of 0.3–2.5 V (vs. Na/Na^+) using a multi-channel battery test system (NEWARE BTS-610). Cyclic voltammetry (CV) was performed on an electrochemical workstation (CHI660D) in the voltage range between 0.3 and 2.5 V (vs. Na/Na^+) at different scanning rates. Electrochemical impedance spectroscopy (EIS) was conducted by applying a perturbation voltage of 5 mV in a frequency range of 10^5 to 10^{-2} Hz on the CHI660D electrochemical workstation.

3. Results and discussion

As shown in Fig. S1, all the diffraction peaks of the as-prepared LTO-C nanosheets can be indexed to the cubic spinel LTO phase structure with a space group of Fd-3m (227) (JCPDS No. 49-0207). The sharp and intense peaks with no impurity peaks confirm the high crystallinity and high-purity of the LTO samples. Fig. S2a shows the representative TEM image of the LTO-C sample revealing the sheet-like morphology. The HR-TEM results acquired from individual nanosheets (see Fig. S2b) disclose the LTO-C nanosheets have high crystallinity and amorphous carbon encapsulation about 2 nm thickness. The TEM elemental map acquired from the LTO-C nanosheets (see Fig. S3) indicates that the carbon encapsulation is homogeneous. Furthermore, TGA analysis (see Fig. S4) reveals that the carbon content in the LTO-C nanosheets is 6.5 wt%.

Fig. 1 illustrates the overall fabrication process of free-standing LTO-C/RGO paper involving modified vacuum filtration and annealing. The prepared LTO-C nanosheets have poor solubility in water thus making it difficult to re-disperse in water to form stable suspensions of LTO-C nanosheets under mechanical stirring (see Fig. S5a). However, in the solution containing NH_4HCO_3 that dissociates easily into cations and anions with high ionic strength around 1 and more than 2 orders of magnitude higher compared to that of pure water, the LTO-C nanosheets have abundant charged ions on the surface and a fine colloid of the LTO-C nanosheets (see Fig. S5b) can be produced without aggregation due to the electrostatic repulsion effect of adjacent nanosheets [30]. This surface charge control of the LTO-C nanosheets in the solution with high ionic strength is important. Previous studies indicate that GO nanosheets prepared by the modified Hummers method are negatively charged in water [31]. This suggests that when the GO nanosheets with negative charges and the LTO-C nanosheets in the solution with high ionic strength are mixed, the LTO-C nanosheets with positive ions tend to be attracted to neutralize the negatively-charged GO, screen the electrostatic repulsion between GO, and eventually disrupt the stability, finally leading to co-assembly and spontaneous co-precipitation of GO and LTO-C nanosheets [31]. As shown in Fig. S5c, after 6 h, black continuous flocculent nanocomposites with a solid-like rheological behavior sink to the bottom rendering the solution colorless visually. The nanocomposite with a uniform color is very stable and no LTO-C nanosheets precipitate implying that a continuously interconnected 3D network based on GO nanosheets without serious stacking and cross-linking LTO nanosheets are produced and tightly attached. Subsequent vacuum-filtration and post-annealing processes afford the formation of freestanding flexible LTO-C/RGO film accompanying the reduction of GO nanosheets and strengthening of internal structure. During annealing, the remaining ammonium salt decomposes readily to provide a nitrogen source for doping of the RGO nanosheets without the introduction of other impurity that adversely affects the performance of the free-standing electrode. As shown in Fig. 1, the LTO-C/RGO film is free-standing and mechanically robust with excellent flexibility (even sustaining 180° bending). The excellent mechanical properties bode well for use as SIB electrodes without the need for a supplementary binder.

The morphology, structure, and composition of the LTO-C/RGO film are characterized by TEM, SEM, XPS, XRD, TGA, and Raman scattering. Fig. 2a depicts the cross-sectional SEM image of the LTO-C/RGO film with a thickness of about 25 μm disclosing the self-supporting nature and good thickness uniformity. The high-magnification SEM image (Fig. 2b) reveals that the confined LTO-C nanosheets are well distributed in the interconnected RGO networks. The results also confirm that the LTO-C nanosheets with positive ions prefer to settle at the functional group sites on the surface and at the periphery of GO nanosheets due to electrostatic screening consequently suppressing self-stacking of GO during co-assembly and spontaneous co-precipitation. The TEM image of the LTO-C/RGO film in Fig. 2c shows that individual LTO-C nanosheet and small aggregates are tightly anchored on the RGO sheets. The crystalline structure of the LTO-C nanosheet is shown in Fig. 2d which reveals the structural conservation of spinel LTO in the fabrication processing. Fig. 3a shows the TGA result and the content of LTO is about 63 wt%.

The phase structures of the LTO-C/RGO film are identified by XRD. As shown in Fig. 3b, besides the peak at 26°, the other sharp and well-defined peaks indicative of high crystallinity can be indexed to spinel LTO according to the standard PDF card data (JCPDS no. 49-0207). The peak at 26° is ascribed to the (002) interlayer diffraction of few-layer RGO nanosheets suggesting that GO has been reduced to RGO in the post-annealing process [32]. The (002) characteristic diffraction peak of RGO in the LTO-C/RGO film is weak and broad, indicating that the RGO sheets are effectively separated by the anchored LTO-C nanosheets. Self-stacking of the RGO layers is suppressed consequently weakening and expanding the reflection peaks. Fig. 3c displays the Raman scattering spectra of the LTO-C/RGO film. Besides the vibration modes from spinel LTO between 300 and 800 cm^{-1}, two distinctive carbon characteristic bands between 1200 can 1700 cm^{-1} can be observed. The asymmetrical shape of the carbon characteristic bands implies the existence of two types of the bonding sates of carbon. The deconvoluted Raman peaks at 1220 and 1522 cm^{-1} are ascribed to short-range vibration of sp^3 carbon [33]. The Raman bands at 1348 and 1589 cm^{-1} correspond to the D and G bands of sp^2 carbon ascribed to the edge planes and disordered structures associated with the disruption of the symmetrical hexagonal graphitic lattice and first-order scattering of the in-plane stretching mode (E_{2g}) for symmetric sp^2 C–C bonds [34], respectively.

The surface chemical composition and electronic states of the LTO-C/RGO film are determined by XPS. The survey XPS spectrum and high-resolution Li 1s, Ti 2p, O, C1s and N1s spectra acquired from the LTO-C/RGO film (Fig. 4a and Fig. S6) reveal the presence of Li, Ti, O, C and N. The high-resolution Li 1s XPS spectrum in the low binding energy region (see Fig. S6) shows a weak Li 1s peak at 54.6 eV from the Li–O bond in the spinel LTO structure. The high-resolution XPS spectrum of Ti 2p reveals two characteristic peaks at 458.7 and 464.2 eV assigned to Ti $2p_{3/2}$ and $2p_{1/2}$, respectively, from titanium in the IV oxidation state. The high-resolution C1s spectrum (see Fig. 4c) shows three deconvoluted peaks at 284.6, 286.1, and 287.5 eV, corresponding to sp^2-hybridized graphitic carbon, oxygen bridged C, and carboxyl C, respectively. Fig. 4d depicts the high-resolution N 1s XPS spectrum and the asymmetrical shape indicates different nitrogen bonding states. The deconvoluted peaks at 398.5, 400.5, and 402.4 eV arise from pyridinic N, pyrrolic N, and protonated N (or graphitic N), respectively. The results indicate that a small amount of carbon in RGO nanosheets has been substituted by nitrogen to improve the conductivity and charge transfer at the interface.

The electrochemical sodium storage characteristics of the flexible LTO-C/RGO film are evaluated by assembling the materials with the appropriate mass in a Na-half cell. Fig. 5a shows the CV curve at

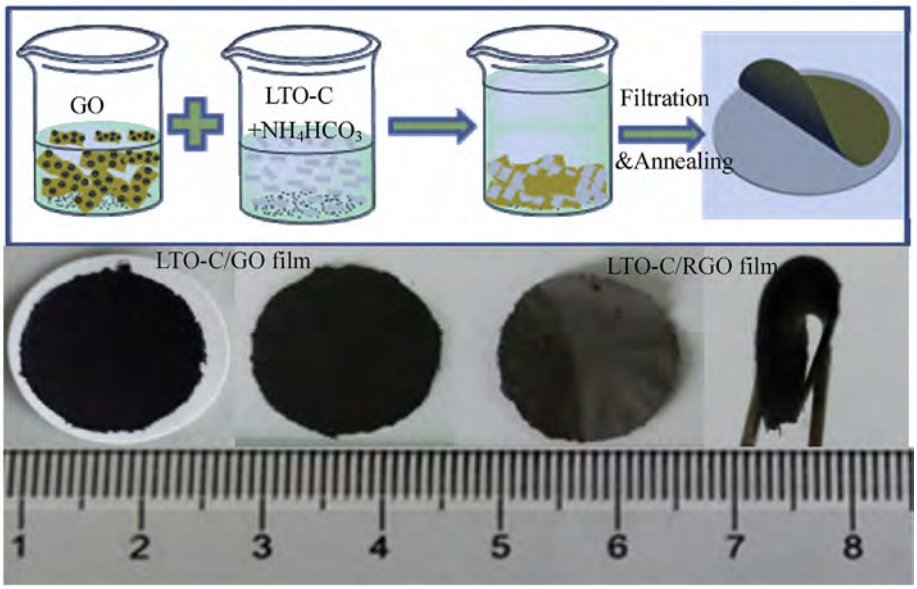

Fig. 1. Schematic of the fabrication procedures and digital images of freestanding LTO-C/RGO film.

a scanning rate of 0.2 mV^{-1} in the potential range between 2.5 and 0.3 V vs. Na^+/Na. A couple of redox peaks located at ~0.67 V (cathodic peak) and ~1.05 V (anodic peak) vs. Na^+/Na can be observed representing typical Na^+ insertion/extraction in the LTO crystal lattice. The strong and well-defined redox peaks of LTO indicate well-behaved electrode kinetics in the LTO-C/RGO film electrode. In previous studies, owing to structural deformation and reconstruction caused by minor surface atomic rearrangements during the redox reaction of Ti^{4+}/Ti^{3+} in spinel LTO upon charging, one anodic peak at ~0.92 V often occurs in the oxidation cycles indicative of poor structural stability [12]. Interestingly, this anodic peak cannot be observed from the LTO-C/RGO film here, implying that hybridizing LTO-C nanosheets with interconnected RGO nanosheets depresses electrochemical atomic rearrangement and improves the structural stability of the LTO crystal lattice during Na^+ insertion/extraction. Fig. 3b shows the typical discharging/charging profiles of the LTO-C/RGO electrode at a current rate of 0.1 C and the Na^+ insertion process can be divided into three domains with a sloping region (I) from open circuit voltage to ~1.05 V, plateau (II) at ~0.75 V, and another sloping region (III) from ~0.75 to 0.3 V. Domains I and II are related to Na^+ insertion into the LTO host lattice whereas Domain III represents interfacial Na storage in the solid–liquid and solid–solid interfaces [20].

The initial discharge and charge capacities of the LTO-C/RGO film are 217 and 193 $mAhg^{-1}$, respectively, which are higher than the theoretical capacity of 175 $mAhg^{-1}$. Similar phenomena have

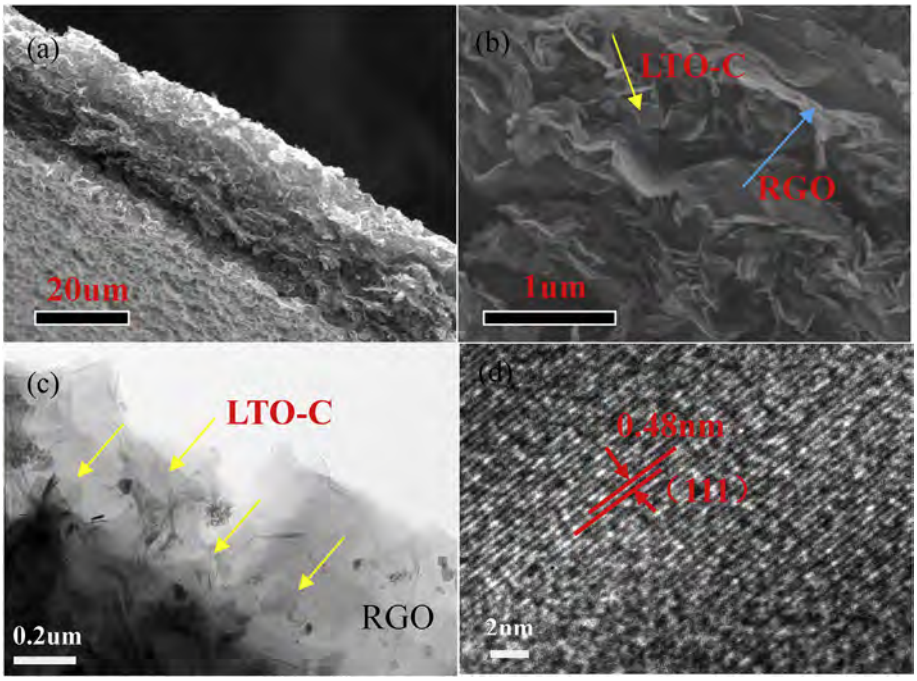

Fig. 2. (a) and (b) Cross-sectional SEM images of the freestanding LTO-C/RGO film; (c) and (d) Representative TEM and HR-TEM images of the freestanding LTO-C/RGO film.

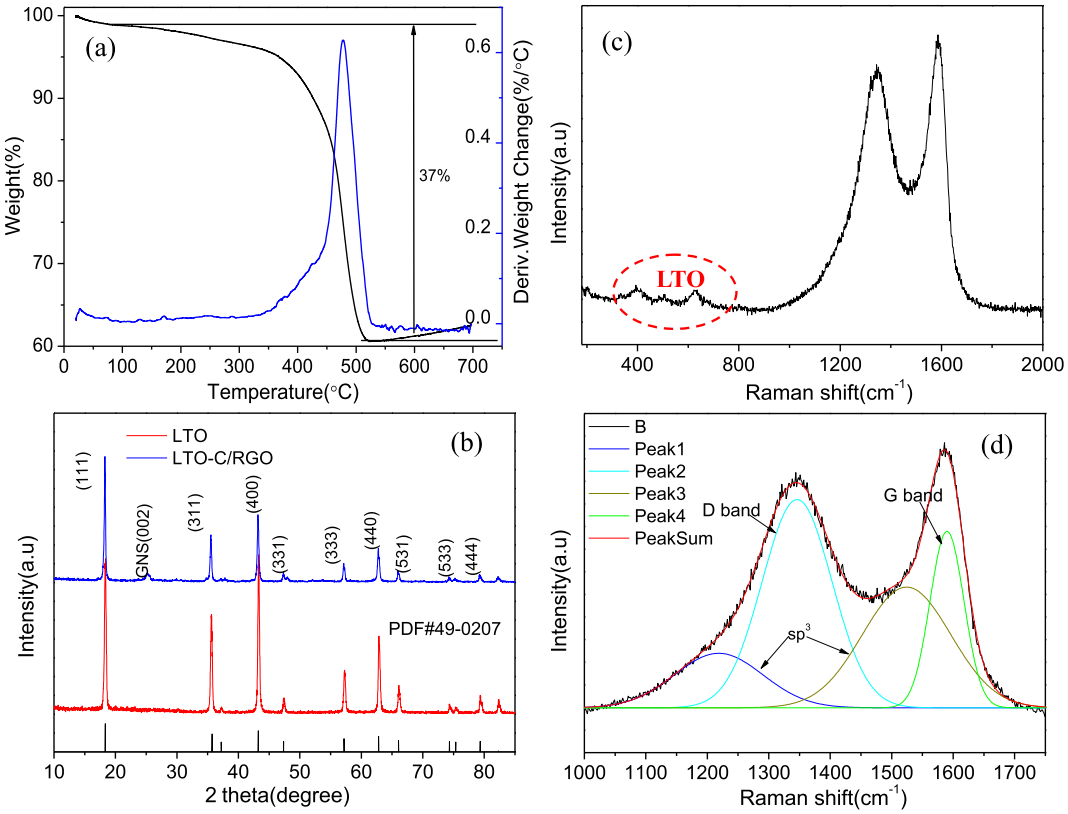

Fig. 3. (a) and (b) TGA curves and XRD patterns of the freestanding LTO-C/RGO film; (c) and (d) Raman scattering spectra of the freestanding LTO-C/RGO film.

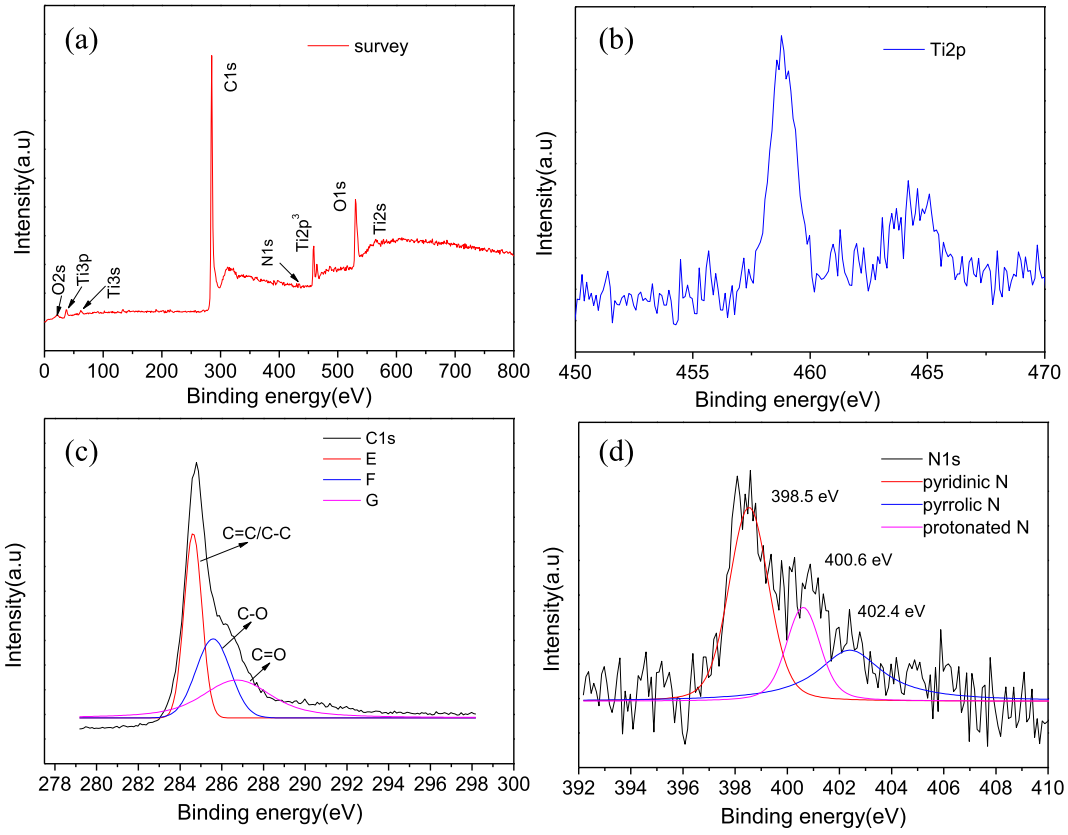

Fig. 4. (a) Survey XPS spectra and (b)–(d) high-resolution Ti 2p, N 1s and C 1s XPS spectra obtained from the freestanding LTO-C/RGO film.

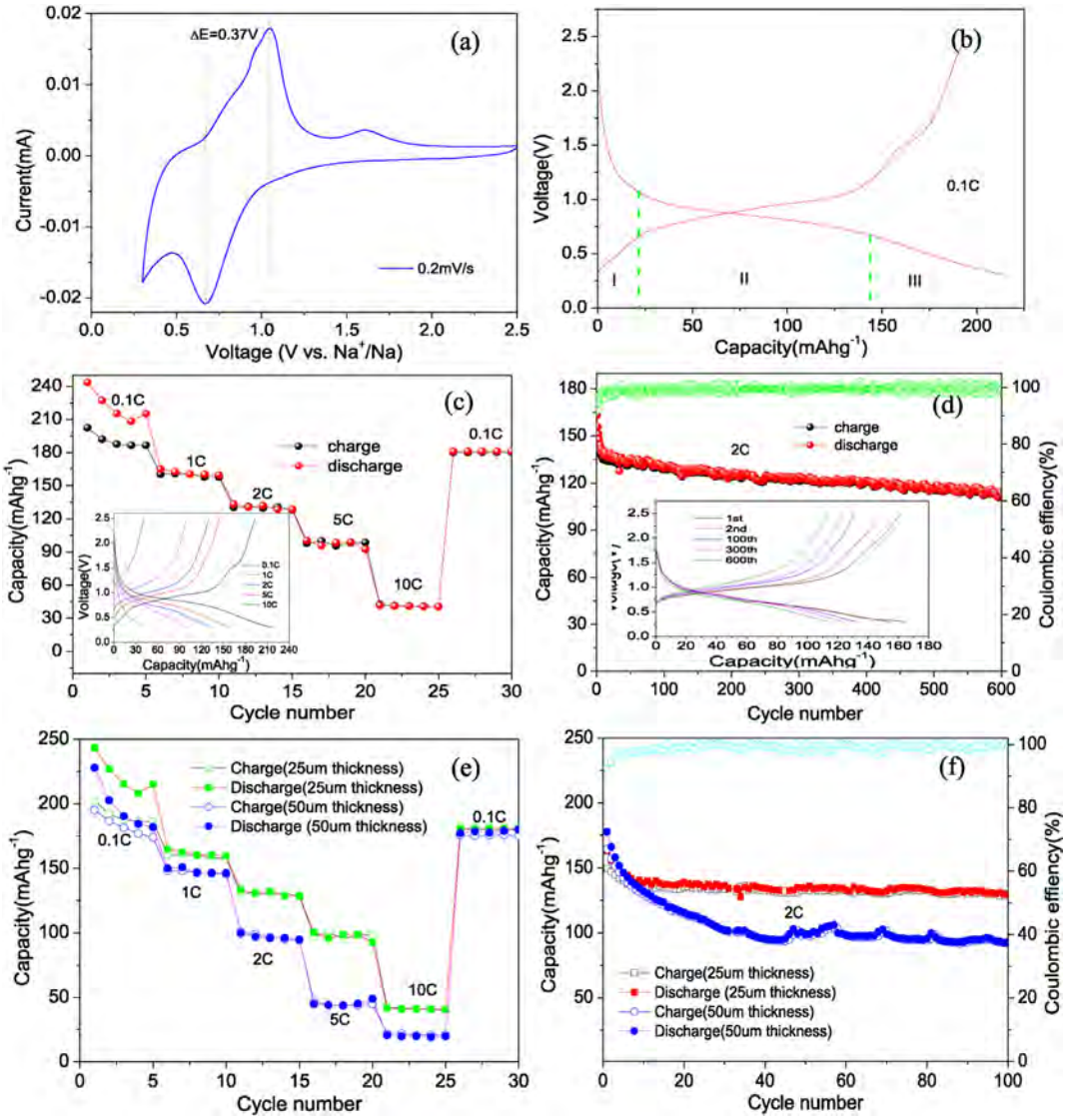

Fig. 5. Electrochemical behavior of the freestanding LTO-C/RGO film with a thickness of 25 μm: (a) Typical CV curve acquired at a scanning rate of 0.2 mV^{-1}; (b) GCD profiles at 0.1 C; (c) Rate performance and GCD profiles (inset) at various current rates; (d) Typical GCD profiles (inset) and cycling performance at 2 C; (e) and (f) Comparison of the rate performance at various current rates and cycling performance at 2 C of the freestanding LTO-C/RGO film electrode with a thicknesses of 25 μm and 50 μm.

been observed from self-assembled TiO_2–graphene hybrid nanostructures [32] and graphene-wrapped porous LTO nanofibers composite [20]. This suggests additional interfacial Na storage in the interface of LTO-C/electrolyte (solid-liquid) and LTO-C/graphene (solid-solid). The sodium storage performance of the LTO-C/RGO film is assessed by cycling at various current densities. As shown in the inset in Fig. 5c, the charging-discharging profiles at different current densities show a similar shape consisting of two sloping regions and one plateau region, indicative of a stable host structure albeit fast Na^+ insertion/extraction. As the current rate is increased, the voltage plateaus decrease apparently, but the sloping region is almost unchanged. These results suggest that Na^+ intercalation into the LTO becomes insufficient at high rates whereas Na^+ adsorption on the interface (interfacial Na storage) is sufficient even at high rates. The LTO-C/RGO film exhibits reversible capacities of 187.6, 161.3, 132.7, and 96.2 at rates of 0.1, 1, 2, and 5 C, respectively. Even at a high rate of 10 C, a reversible capacity of 42.5 $mAhg^{-1}$ is retained. When the current rate is reset to 0.1 C after cycling at various rates, the capacity can recover to 181 $mAhg^{-1}$. The results show that the LTO-C/RGO film have superior rate capability and good cyclability.

With regard to the cycling durability, the cycling performance is investigated at a large current density of 2 C. After a fast decay in the initial 10 cycles, the LTO-C/RGO film anode shows a stable capacity of 140 $mAhg^{-1}$ with high Coulombic efficiency approaching 100%. It retains a capacity of 114 $mAhg^{-1}$ after 600 cycles with a capacity loss below 0.04% per cycle. To the best of our knowledge, this is the first time such a high-rate and long cycle-life performance have been achieved from flexible LTO materials as anodes in Na ion storage. The morphology of the LTO-C/RGO electrode after cycling for 600 times are shown in Fig. 6a and b. There is no apparent difference between the SEM images after cycling and the RGO sheets are in good contact with adjacent LTO-C nanosheets. The crystalline structure of the LTO-C/RGO electrode after cycling is also investigated by Raman scattering. As shown in Fig. 6c, besides the strong Raman peak from carbon, the characteristic peaks corresponding to the stretching vibrational mode of the Ti–O covalent bond in the TiO_6 octahedra at 670 cm^{-1} and stretching vibrational mode of the Li–O ionic bond located in the LiO_4 tetrahedra at 431 cm^{-1} from spinel LTO are identified. The results show that the

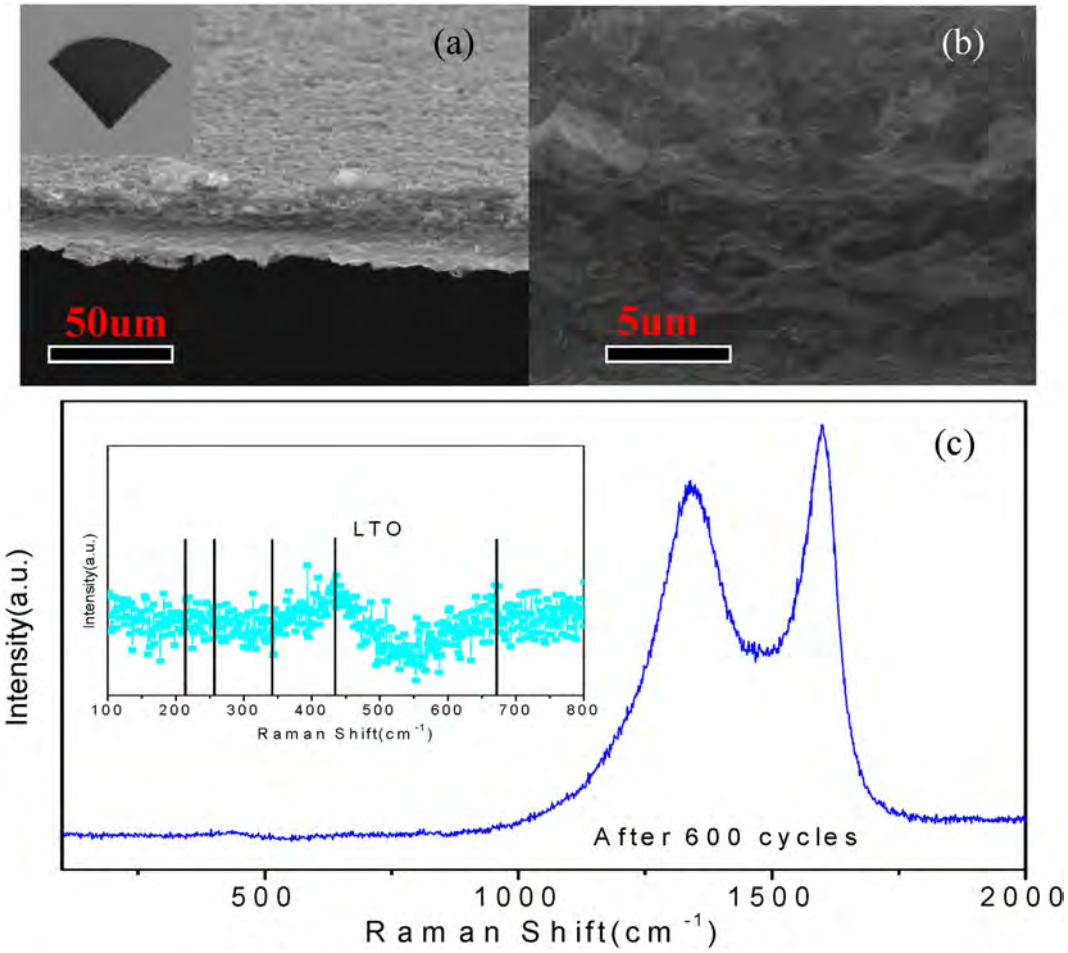

Fig. 6. (a) and (b) Photograph and SEM image of the freestanding LTO-C/RGO film with a thickness of 25 μm after 600 cycles at 2 C; (c) Raman scattering spectra acquired from the freestanding LTO-C/RGO film after 600 cycles at 2 C.

LTO-C/RGO electrode is robust and can sustain long-term cycling.

From the practical viewpoint, it is recognized that areal mass loading is required for high-performance electrodes. On the basis of the flexibility resulting from the LTO-C/RGO fabrication process in conjunction with increased electrode thickness and thus areal mass loading, the electrochemical sodium storage performance of LTO-C/RGO film with a thickness up to 50 μm (Fig. S7) or twice the areal mass loading is evaluated. As shown in Fig. 5e and f, at a rate of 2 C, the thick LTO-C/RGO electrode still delivers competitive performance with a capacity of 95 $mAhg^{-1}$ and good durability with a capacity of 91 $mAhg^{-1}$ after 100 cycles. In principle, stable cycling of an electrode with high material mass loading requires structural uniformity in the entire electrode because even small changes evoking local inhomogeneity can accumulate across the thickness of the electrode and degrade the electrode. Table SI shows the charge-transfer resistance (R_{ct}) of the LTO-C/RGO electrode according to Nyquist plots (see Fig. S8) based on EIS after the rate capability test. Using the inset equivalent circuit model, the calculated R_{ct} values for the LTO-C/RGO electrodes with thicknesses of 25 μm and 50 μm are 196.5 and 231.9Ω, respectively. The small difference in R_{ct} between the thin and thick electrodes is an indication of the highly effective charge transfer process at the electrode/electrolyte interface, thereby confirming that the rapid transport kinetics during discharging and charging is responsible for the superior Na storage.

Considering the flexibility of the involved fabrication protocol, the above results are indicative of potential application of the LTO-C/RGO film in high-performance SIBs for portable, flexible and wearable electronics. The outstanding electrochemical performance can be attributed to the unique architecture of the 2D LTO-C nanosheets and highly conductive interconnected RGO networks. Firstly, the planar structure of the LTO-C nanosheets with ultrathin carbon encapsulation not only increases the specific surface area for Na^+ insertion/extraction, shortens the ion diffusion pathways and promotes the charge transfer/collection kinetics, but also improves the structural strength and electrochemical stability of the spinel LTO. Secondly, the conductive interconnected RGO networks lead to fast charge transport to lower the resistance for Na storage and act as a substrate to buffer the volume change during Na-ion insertion/extraction benefiting long-cycling stability. Thirdly, the strong adhesion between the LTO-C nanosheets and RGO networks offers abundant interfacial sites for Na adsorption, which is beneficial to Na insertion/extraction and additional interfacial Na storage. Fig. 7a shows the CV curves of the LTO-C/RGO film with a thickness of 25 μm at different scan rates. With increasing scanning rates, the redox peak separation increases, indicating that a higher energy is needed for Na^+ intercalation at a higher rate. In general, the currents (i) in the CV curves of the active electrode materials responding to the sweeping rates (υ) obey a power law relationship of $i = a\upsilon^b$, where a and b are adjustable values [35,36]. If $b = 1$, the total charge (Q) comes from the capacitive process (interfacial Na storage process) and if $b = 0.5$, it is totally diffusion-controlled (Na^+

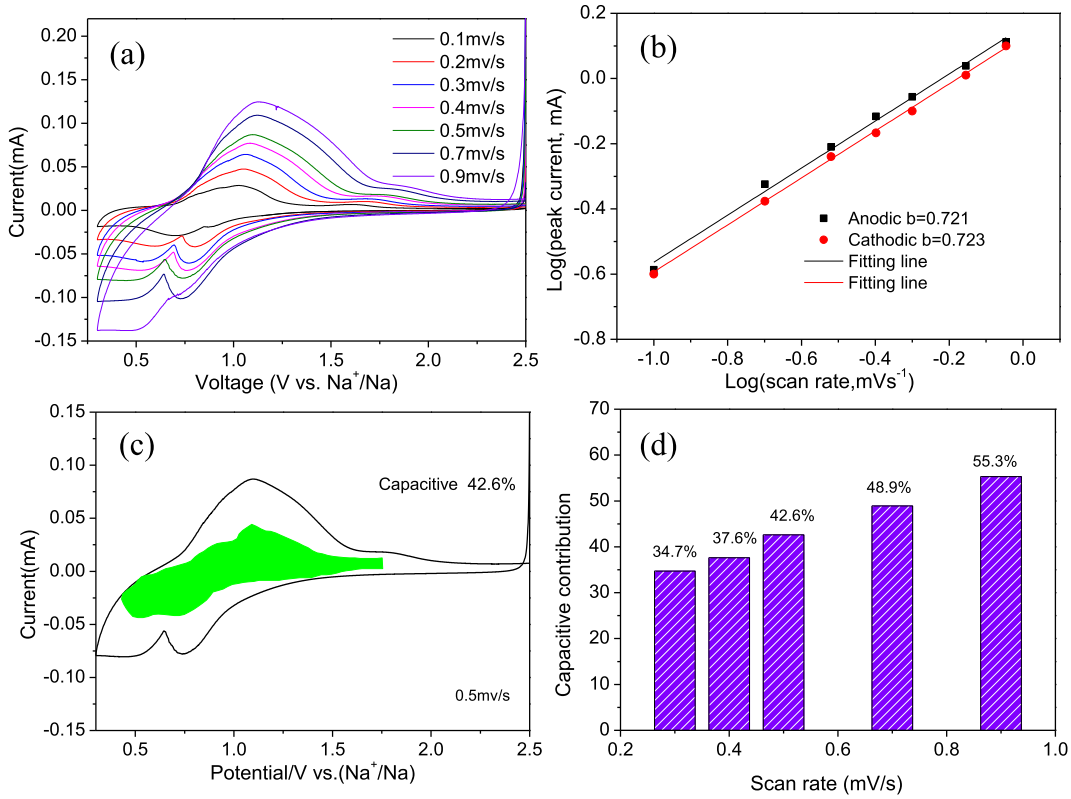

Fig. 7. Kinetic analysis of the freestanding LTO-C/RGO film electrode with a thicknesses of 25 μm: (a) CV curves and (b) Corresponding Log (scan rate)-Log (peak current) profiles at scanning rates between 0.1 and 0.9 mV/s. (c) Separation of the capacitive charge from the total charge at 0.5 mV/s; (d) Comparison between the capacitive charge contributions of various scanning rates.

insertion/extraction process). Fig. 7b present the log(v)-log(i) plots for the LTO-C/RGO film and the fitted b values for the cathodic and anodic peak currents are 0.723 and 0.721, respectively, implying that the charge (thus the capacity) comes from two contributions. The exact ratio between the two contributions at a certain scanning rate by separating the specific contribution from the capacitive (interfacial Na storage process) and diffusion-controlled (Na^+ insertion/extraction process) charge at a particular voltage can be determined according to following equations [37],

$$i(V) = k_1 v + k_2 v^{1/2} \quad (1)$$

and

$$i(V)/v^{\frac{1}{2}} = k_1 v^{\frac{1}{2}} + k_2 \quad (2)$$

where $k_1 v$ and $k_2 v^{1/2}$ denote the contributions from capacitive effect and intercalation process, respectively. The parameters of k_1 and k_2 are fitted according to Equation (2) (see S9 and Table SII), and the corresponding current contribution as a function of potential can be obtained. Then, the CV curve for Na^+ storage is displayed (for example, at scan rate of 0.5 mV/s, see Fig. 7c), in which, the capacitive currents ($k_1 v$) are plotted and distinguished from the total measured currents. As a result, the amount of stored charge (Q) around the redox peaks from the capacitive contribution is calculated by integrating green area according to the following equation:

$$Q = \int (i/v) dV \quad (3)$$

As shown in Fig. 7c, the capacitive (interfacial) contribution is determined to be 42.6% at 0.5 mV/s, suggesting that Na storage in the LTO-C/RGO film is generated by both the capacitive (interfacial) and diffusion-controlled (intercalation) processes. The capacitive (interfacial) contributions increase from 34.7% to 55.3% as the scanning rates are increased from 0.3 to 0.9 mV/s (see Fig. 7d). This indicates that the kinetics of Na^+ intercalation process is limited at high rates but the kinetics of interfacial Na storage is still sufficient. It is consistent with the aforementioned sodium storage performance observed from the LTO-C/RGO film at various current densities. The CV analysis corroborates the effect of confining that the LTO-C nanosheets in the conductive interconnected RGO networks endow the LTO-C/RGO film with both the intercalation-based and interfacial Na storage behavior thereby accounting for the high capacity, superior rate capability, and long cycle life demonstrated in this study.

4. Conclusion

Free-standing and robust LTO-C/RGO electrodes are prepared by modified vacuum filtration and annealing. During the fabrication, the GO nanosheets with negative charges and LTO-C nanosheets with abundant charged ions are self-assembled into the nanocomposites as a result of electrostatic screening. The unique structure of the confined LTO-C nanosheets in highly conductive interconnected RGO networks not only promotes the reaction kinetics and structural stability of the electrodes during Na^+ insertion/extraction, but also provides abundant LTO-C/electrolyte and LTO-C/graphene interfacial sites for Na^+ adsorption, giving rise to additional interfacial Na storage. In the evaluation as an anode for SIBs, the flexible LTO-C/RGO electrode delivers a high reversible

capacity of 166 $mAhg^{-1}$ at 1 C, good rate capability of 98.7 $mAhg^{-1}$ at 5 C, and superior cyclic performance of 114 $mAhg^{-1}$ at 2 C after 600 cycles. In conjunction with the simple and flexible fabrication protocol, the LTO-C/RGO film with superior Na storage performance has large potential in high-performance SIBs for portable, flexible and wearable electronics.

Acknowledgements

This work was financially supported by the Grants from National Natural Science Foundation of China (Nos. 11474242, 51272220 and 51472209), Program for Changjiang Scholars and Innovative Research Team in University (IRT13093), the Hunan Provincial Innovation Foundation for Graduate (No. CX2016B254) and City University of Hong Kong Applied Research Grant (ARG) No. 9667122.

Appendix A. Supplementary data

Supplementary data related to this article can be found at http://dx.doi.org/10.1016/j.jpowsour.2016.10.088.

References

[1] M.F. El-Kady, V. Strong, S. Dubin, R.B. Kaner, Science 335 (2012) 1326–1330.
[2] X. Wang, X. Lu, B. Liu, D. Chen, Y. Tong, G. Shen, Adv. Mater. 26 (2014) 4763–4782.
[3] X. Xiang, K. Zhang, J. Chen, Adv. Mater. 27 (2015) 5343–5364.
[4] N. Yabuuchi, K. Kubota, M. Dahbi, S. Komaba, Chem. Rev. 114 (2014) 11636–11682.
[5] M. Armand, J.-M. Tarascon, Nature 451 (2008) 652–657.
[6] T.-F. Yi, S.-Y. Yang, Y. Xie, J. Mater. Chem. A 3 (2015) 5750–5777.
[7] X. Lu, L. Zhao, X. He, R. Xiao, L. Gu, Y.S. Hu, H. Li, Z. Wang, X. Duan, L. Chen, Adv. Mater. 24 (2012) 3233–3238.
[8] Y. Sun, L. Zhao, H. Pan, X. Lu, L. Gu, Y.-S. Hu, H. Li, M. Armand, Y. Ikuhara, L. Chen, Nat. Commun. 4 (2013) 1870.
[9] G. Xu, L. Yang, X. Wei, J. Ding, J. Zhong, P.K. Chu, Adv. Funct. Mater. 26 (2016) 3349–3358.
[10] P. Yu, C. Li, X. Guo, J. Phys. Chem. C 118 (2014) 10616–10624.
[11] X. Yu, H. Pan, W. Wan, C. Ma, J. Bai, Q. Meng, S.N. Ehrlich, Y.-S. Hu, X.-Q. Yang, Nano Lett. 13 (2013) 4721–4727.
[12] G. Hasegawa, K. Kanamori, T. Kiyomura, H. Kurata, K. Nakanishi, T. Abe, Adv. Energy Mater. 5 (2015) 1400730.
[13] L. Yu, H.B. Wu, X.W.D. Lou, Adv. Mater. 25 (2013) 2296–2300.
[14] Y.-Q. Wang, L. Gu, Y.-G. Guo, H. Li, X.-Q. He, S. Tsukimoto, Y. Ikuhara, L.-J. Wan, J. Am. Chem. Soc. 134 (2012) 7874–7879.
[15] K.-T. Kim, C.-Y. Yu, C.S. Yoon, S.-J. Kim, Y.-K. Sun, S.-T. Myung, Nano Energy 12 (2015) 725–734.
[16] J. Liu, K. Song, P.A. van Aken, J. Maier, Y. Yu, Nano Lett. 14 (2014) 2597–2603.
[17] Y. Ma, B. Ding, G. Ji, J.Y. Lee, ACS Nano 7 (2013) 10870–10878.
[18] Y. Yang, B. Qiao, X. Yang, L. Fang, C. Pan, W. Song, H. Hou, X. Ji, Adv. Funct. Mater. 24 (2014) 4349–4356.
[19] H.-G. Jung, S.-T. Myung, C.S. Yoon, S.-B. Son, K.H. Oh, K. Amine, B. Scrosati, Y.-K. Sun, Energy & Environ. Sci. 4 (2011) 1345–1351.
[20] C. Chen, H. Xu, T. Zhou, Z. Guo, L. Chen, M. Yan, L. Mai, P. Hu, S. Cheng, Y. Huang, Adv. Energy Mater. 6 (2016), 201600322.
[21] M. Zhou, X. Li, B. Wang, Y. Zhang, J. Ning, Z. Xiao, X. Zhang, Y. Chang, L. Zhi, Nano Lett. 15 (2015) 6222–6228.
[22] C. Zhu, P. Kopold, P.A. van Aken, J. Maier, Y. Yu, Adv. Mater. 28 (2016) 2409–2416.
[23] F. Bonaccorso, L. Colombo, G. Yu, M. Stoller, V. Tozzini, A.C. Ferrari, R.S. Ruoff, V. Pellegrini, Science 347 (2015) 1246501.
[24] C. Lai, Y. Dou, X. Li, X. Gao, J. Power Sources 195 (2010) 3676–3679.
[25] N. Li, G. Zhou, F. Li, L. Wen, H.M. Cheng, Adv. Funct. Mater. 23 (2013) 5429–5435.
[26] S. Chen, Y. Xin, Y. Zhou, Y. Ma, H. Zhou, L. Qi, Energy & Environ. Sci. 7 (2014) 1924–1930.
[27] C. Han, Y. He, B. Li, H. Li, J. Ma, H. Du, X. Qin, Q. Yang, F. Kang, ChemSusChem 7 (2014) 2567–2574.
[28] G. Xu, W. Li, L. Yang, X. Wei, J. Ding, J. Zhong, P.K. Chu, J. Power Sources 276 (2015) 247–254.
[29] L. Wen, F. Li, H.M. Cheng, Adv. Mater. 28 (2016) 4306–4337.
[30] Y. Tang, Y. Zhang, X. Rui, D. Qi, Y. Luo, W.R. Leow, S. Chen, J. Guo, J. Wei, W. Li, Adv. Mater. 28 (2016) 1567–1576.
[31] J. Rong, M. Ge, X. Fang, C. Zhou, Nano Lett. 14 (2013) 473–479.
[32] S. Yu, L. Yang, Y. Tian, P. Yang, F. Jiang, S. Hu, X. Wei, J. Zhong, J. Mater. Chem. A 1 (2013) 12750–12758.
[33] Z. Ding, L. Zhao, L. Suo, Y. Jiao, S. Meng, Y.-S. Hu, Z. Wang, L. Chen, Phys. Chem. Chem. Phys. 13 (2011) 15127–15133.
[34] H. Cao, B. Li, J. Zhang, F. Lian, X. Kong, M. Qu, J. Mater. Chem. 22 (2012) 9759–9766.
[35] B. Wang, X. Li, B. Luo, L. Hao, M. Zhou, X. Zhang, Z. Fan, L. Zhi, Adv. Mater. 27 (2015) 1526–1532.
[36] V. Augustyn, J. Come, M.A. Lowe, J.W. Kim, P.-L. Taberna, S.H. Tolbert, H.D. Abruña, P. Simon, B. Dunn, Nat. Mater. 12 (2013) 518–522.
[37] G.A. Muller, J.B. Cook, H.-S. Kim, S.H. Tolbert, B. Dunn, Nano Lett. 15 (2015) 1911–1917.

Electronic Supplementary Information

Free-standing Electrodes Composed of Carbon-Coated $Li_4Ti_5O_{12}$ Nanosheets and Reduced Graphene Oxide for Advanced Sodium Ion Batteries

GuobaoXu[a], Ye Tian[a], Xiaolin Wei[a], Liwen Yang[a,b*], Paul K Chu[b]*

[a] *Hunan Key Laboratory of Micro-Nano Energy Materials and Devices and School of Physics and Optoelectronics, Xiangtan University, Hunan 411105, China*

[b] *Department of Physics and Materials Science, City University of Hong Kong, Tat Chee Avenue, Kowloon, Hong Kong, China*

* Corresponding authors: ylwxtu@xtu.edu.cn (L.W. Yang); paul.chu@cityu.edu.hk (P.K. Chu)

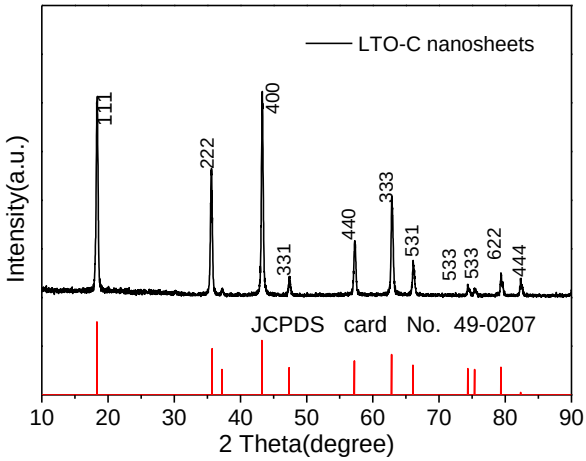

Figure S1. XRD spectrum of the LTO-C nanosheets.

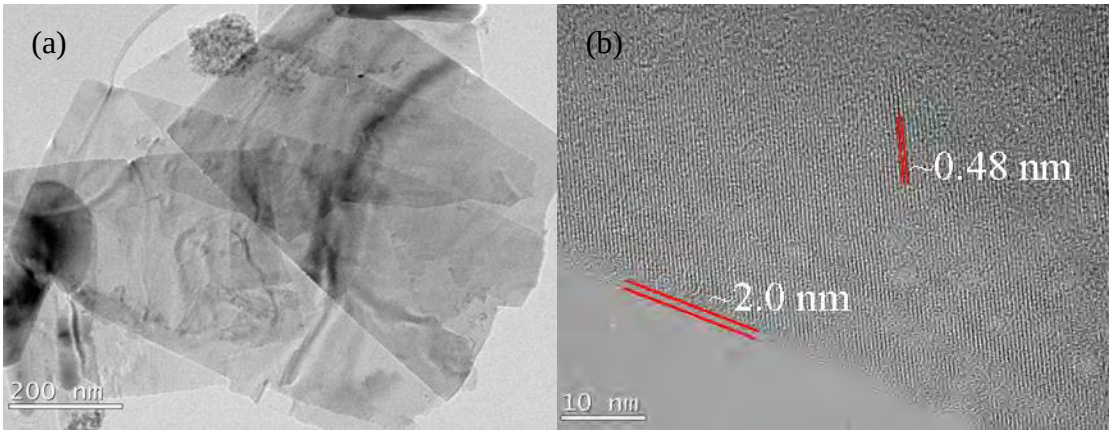

Figure S2. (a) TEM and (b) HR-TEM images of the LTO-C nanosheets.

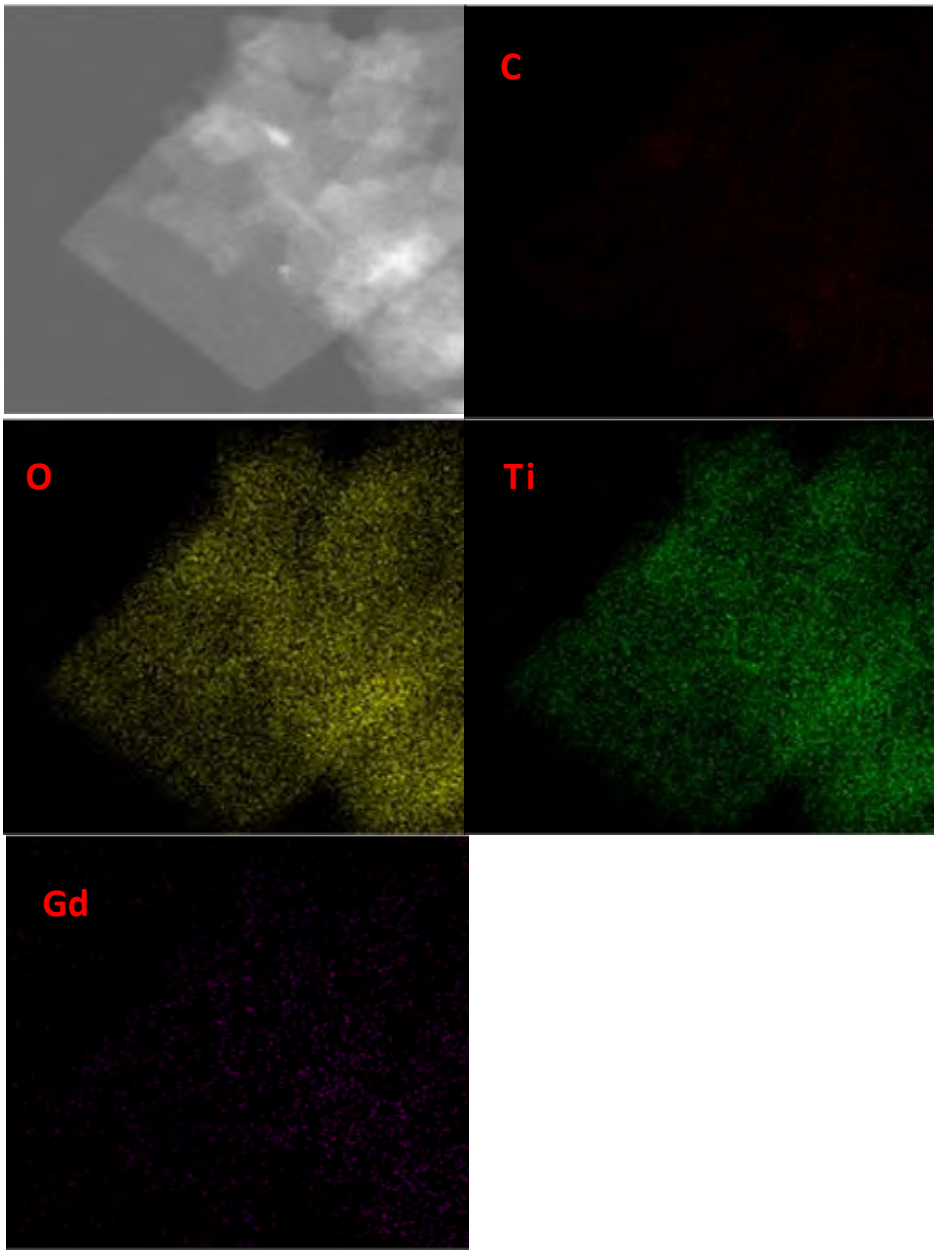

Figure S3. TEM elemental maps acquired from the LTO-C nanosheets.

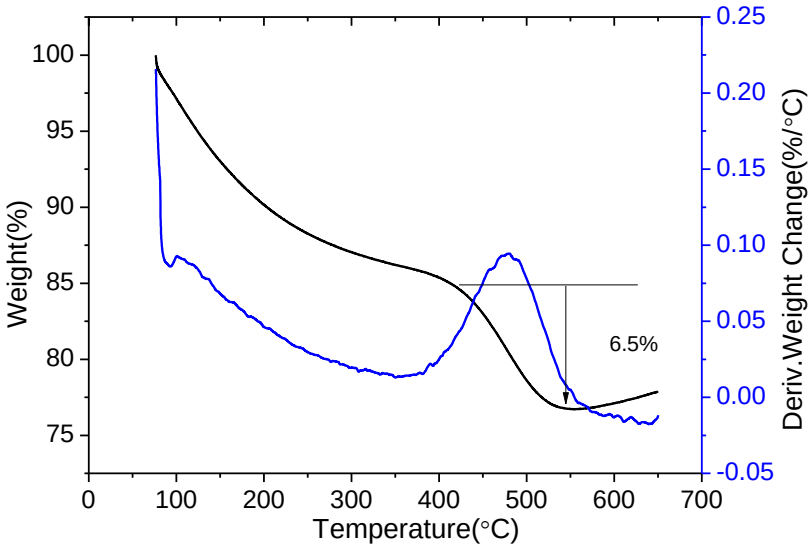

Figure S4. TGA-DSC curves of the LTO-C nanosheets.

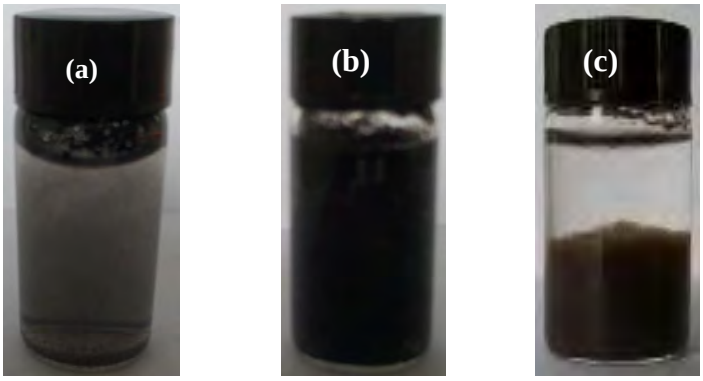

Figure S5: (a) and (b) Optical photographs of the LTO-C nanosheets dispersed in water and the solution with 1 M NH_4HCO_3, respectively; (c) Optical photograph of the flocculent LTO-C/GO nanocomposite.

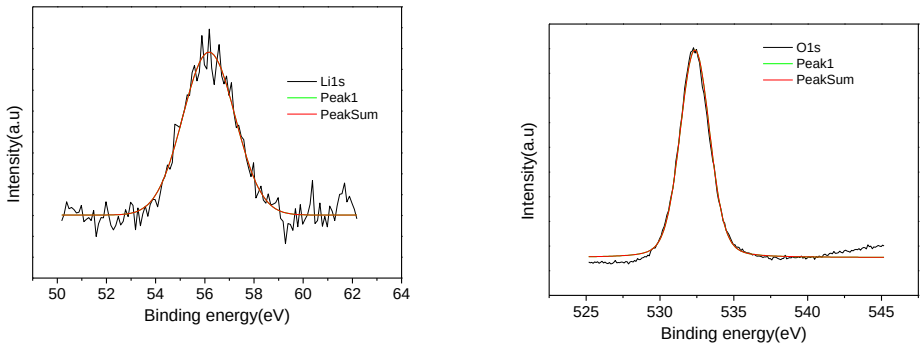

Figure S6: High-resolution (a) Li 1s and (b) O 1s XPS spectra.

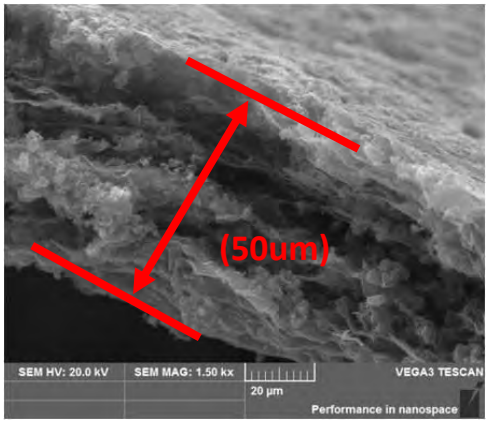

Figure S7: SEM image of the LTO-C/RGO film with a thickness of 50 µm.

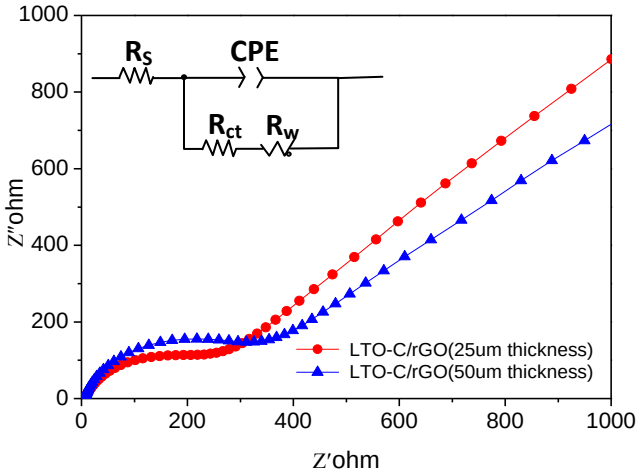

Figure S8: Nyquist plots of the LTO-C/RGO films with thicknesses of 25 and 50 µm.

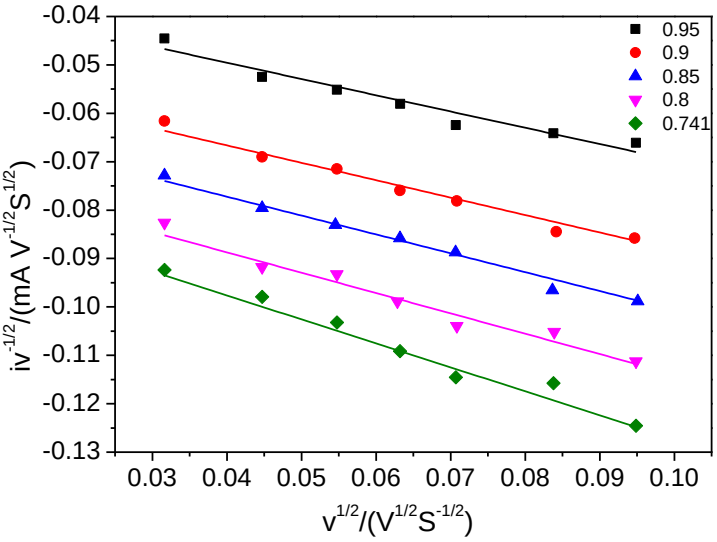

Figure S9 $iv^{-1/2}$ vs. $v^{1/2}$ at different Na^+ reaction potentials around the cathodic peak and its linear fitting using the equation of $i(V)/v^{1/2} = k_1 v^{1/2} + k_2$

Table SI. R_s and R_{ct} values of the LTO-C/RGO electrodes with thicknesses of 25 and 50 µm in half-cells according to **Figure S8** and the inset equivalent circuit model.

	R_s	R_{ct}
CLTO-rGO-(50um)	7.316	231.9
CLTO-rGO-(25um)	5.16	196.5

Table SII. k_1 and k_2 values obtained by the linear fitting of $iv^{-1/2}$ vs. $v^{1/2}$ plots at different Na^- reaction potentials (V) as shown in S9 according to $i(V)/v^{1/2} = k_1 v^{1/2} + k_2$, where i and v are the measured current and scan rate respectively.

Potential/V vs.(Na^+/Na)	K_1[X10^{-4}/(AV^{-1} s)]	K_2[X10^{-5}/(A $V^{-1/2}$ $s^{1/2)}$]
0.741	-4.95	-7.78
0.8	-4.20	-7.19
0.85	-3.897	-6.16
0.90	-3.6	-5.22
0.95	-3.36	-3.61